Stellar (n,γ) cross sections of p-process isotopes. II. ^{168}Yb, ^{180}W, ^{184}Os, ^{190}Pt, and ^{196}Hg

J. Marganiec[*]
Karlsruhe Institute of Technology (KIT), Campus Nord, Institut für Kernphysik, Karlsruhe, Germany, and University of Lodz, Division of Nuclear Physics, Lodz, Poland

I. Dillmann[†]
II. Physikalisches Institut, Justus-Liebig-Universität Giessen, D-35392 Giessen, Germany, and GSI Helmholtzzentrum für Schwerionenforschung GmbH, Planckstrasse 1, D-64291 Darmstadt, Germany

C. Domingo Pardo[‡]
GSI Helmholtzzentrum für Schwerionenforschung GmbH, Planckstrasse 1, D-64291 Darmstadt, Germany

F. Käppeler and S. Walter
Karlsruhe Institute of Technology (KIT), Campus Nord, Institut für Kernphysik, Karlsruhe, Germany
(Received 24 February 2010; revised manuscript received 30 August 2010; published 29 September 2010)

The neutron-capture cross sections of ^{168}Yb, ^{180}W, ^{184}Os, ^{190}Pt, and ^{196}Hg have been measured by means of the activation technique. The samples were irradiated in a quasistellar neutron spectrum of $kT = 25$ keV, which was produced at the Karlsruhe 3.7-MV Van de Graaff accelerator via the ^{7}Li$(p,n)^{7}$Be reaction. Systematic uncertainties were investigated in repeated activations with different samples and by variation of the experimental parameters, that is, irradiation times, neutron fluxes, and γ-ray counting conditions. The measured data were converted into Maxwellian-averaged cross sections at $kT = 30$ keV, yielding 1214 ± 61, 624 ± 54, 590 ± 43, 511 ± 46, and 201 ± 11 mb for ^{168}Yb, ^{180}W, ^{184}Os, ^{190}Pt, and ^{196}Hg, respectively. The present results either represent first experimental data (^{168}Yb, ^{184}Os, and ^{196}Hg) or could be determined with significantly reduced uncertainties (^{180}W and ^{190}Pt). These measurements are part of a systematic study of stellar (n,γ) cross sections of the stable p isotopes.

DOI: 10.1103/PhysRevC.82.035806 PACS number(s): 25.40.Lw, 26.30.Ef, 27.70.+q, 27.80.+w

I. INTRODUCTION

Almost all nuclei heavier than Fe are formed by neutron-capture processes, with the exception of 32 proton-rich stable isotopes between ^{74}Se and ^{196}Hg [1,2]. These isotopes cannot be produced by the s- and r-processes, because they are either outside the s-process path or shielded by stable isotopes against the β^--decay chains from the r-process region (Fig. 1).

The nature of the p-process is still under debate. However, in the current understanding the p-process abundances seem to originate from a superposition of several processes. The largest fraction can be explained with the "γ-process" during type II supernovae [3–5], but for the missing abundances additional processes (rp-process [6,7], ν-process [8], νp-process [9]) have been postulated (for a more detailed discussion, see Part I [10] of this series of articles).

In the γ-process the Ne/O layers are heated during the explosion by the outgoing shock front to ignition temperatures of explosive burning. When the temperature in the Ne/O shell reaches values of 2–3 GK, photodisintegration processes shift the existing seed nuclei by a sequence of (γ,n) reactions to the proton-rich side of the valley of stability. In each step, the neutron separation energy grows progressively, while the separation energy for protons and α particles is decreasing. Consequently, when (γ,p) and (γ,α) reactions become comparable or faster than (γ,n), the reaction path is deflected from the initial isotopic chain and feeds nuclei with lower atomic number Z. The competition between (γ,n), (γ,p), and (γ,α) reactions gives rise to an extended network connecting about 2000 nuclei with more than 10 000 reactions [11]. While photodisintegration dominates in the early, hot phase, the initially released neutrons can be recaptured at a later time, when the material cools down after the passage of the shock wave. At the end of the γ-process, when the shock front has passed the Ne/O shell, the temperature and density drop exponentially and the unstable proton-rich nuclei decay back to the valley of stability, thus producing the p nuclei together with minor contributions to the s and r abundances. The typical p-process abundance pattern exhibits maxima at ^{92}Mo ($N = 50$) and ^{144}Sm ($N = 82$).

This is the second article of a series describing activation measurements on the neutron-deficient and neutron-rich side of the stability valley and it follows a recent publication by Dillmann *et al.* [10]. The present work is motivated by the twofold role of neutron reactions in the p-process. Free neutrons liberated in (γ,n) reactions are recaptured

[*]Now at GSI Helmholtzzentrum für Schwerionenforschung GmbH, Planckstrasse 1, D-64291 Darmstadt Germany; j.marganiec@gsi.de
[†]Previously at Karlsruhe Institute of Technology (KIT), Campus Nord, Institut für Kernphysik, Karlsruhe, Germany and Physik Department E12 and Excellence Cluster Universe, Technische Universität München, Germany.
[‡]Previously at Karlsruhe Institute of Technology (KIT), Campus Nord, Institut für Kernphysik, Karlsruhe, Germany.

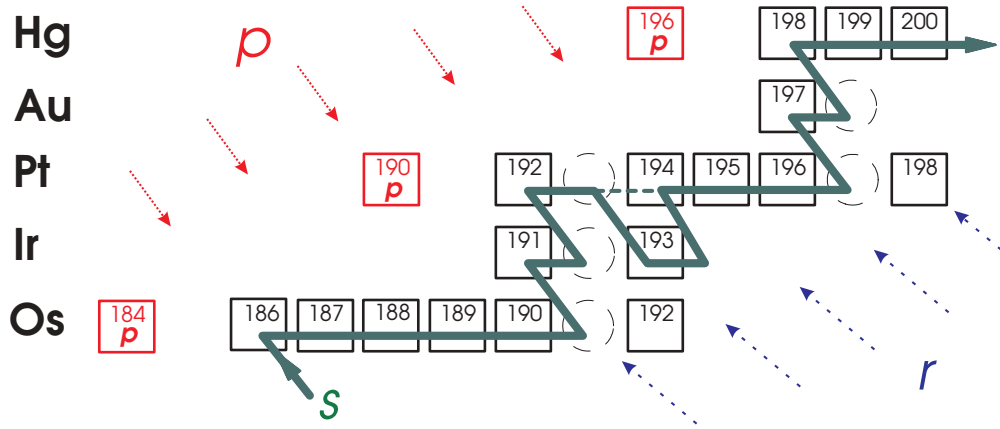

FIG. 1. (Color online) Example from the chart of nuclides illustrating the neutron-capture origin of most stable isotopes, which are either produced directly by the s-process and/or by the β^--decay chains from the r-process region. Exceptions are the few stable nuclei on the proton-rich side of the stability valley, which are made by photodisintegration reactions in the p-process.

and thus contribute to the reaction network. This aspect is most important during freeze-out, when the neutron density decreases. Furthermore, neutron cross sections are important because direct and backward reactions are connected by detailed balance. Therefore, (n,γ) cross sections can be used to infer the corresponding (γ,n) rates.

In view of the huge number of reactions in the p-process network, predominantly between unstable nuclei, it is obvious that the vast majority of these rates have to rely on theoretical calculations and that the predictive power of such calculations is crucial for the reliability of the derived p abundances. As is shown in Ref. [12] the cross section trend with neutron number for long isotope chains provides a sensitive test for the extrapolation into the region of unstable nuclei. Examples are the elements Yb, Os, and Hg, all with seven stable isotopes, where experimental values for the cross sections of the respective p isotopes are still missing. For W and Pt this trend is obscured by large cross-section uncertainties of 10% and 25% for the p nuclei ^{180}W and ^{190}Pt [13].

Another motivation is the fact that self-consistent studies of the γ-process have problems with synthesizing the p-nuclei in the mass regions $A < 124$ and $150 \leqslant A \leqslant 165$ [14]. This may result from difficulties related to the astrophysical models as well as from systematic uncertainties of the nuclear physics input. Therefore, the improvement of nuclear-reaction cross sections is crucial for further progress in p-process models, either by directly replacing theoretical predictions by experimental data or by testing the reliability of predictions if the relevant energy range is not accessible by experiments.

In this context we have carried out an extensive experimental program to measure the (n,γ) cross sections of 13 p-only isotopes by means of the activation technique [10,12,15]. The present article completes this series of measurements with the isotopes ^{168}Yb, ^{180}W, ^{184}Os, ^{190}Pt, and ^{196}Hg. A concluding article will then present p-process network calculations based on a new version of the Karlsruhe Astrophysical Database of Nucleosynthesis in Stars (KADoNiS) [16,17], where the available experimental and semiempirical (n,γ) cross sections for the p-process will be added to the already existing data library. These data will necessarily remain a complement to the indispensable theoretical predictions for the vast majority of the mostly unstable isotopes in the p-process network, which are not accessible to cross section measurements with present experimental techniques. Nevertheless, these data provide important tests of existing calculations in the Hauser-Feshbach statistical model [18], that is, with the codes NON-SMOKER [19,20] or MOST [21].

The measurements and data analysis are described in Secs. II and III. The results and their impact for the p-process network are presented in Sec. IV.

II. MEASUREMENT OF STELLAR (n,γ) CROSS SECTIONS

A. Neutron irradiation setup

The present measurements of stellar (n,γ) cross sections are based on the activation technique, which consists of the irradiation of a sample in a well-defined neutron spectrum and the subsequent determination of the induced γ activities. This method is known to be very sensitive and selective [22] and allows one to perform accurate measurements, even of small cross sections and very small samples.

Neutrons were produced by bombarding thin layers of LiF with protons of $E_p = 1912$ keV, about 31 keV above the threshold of the ^{7}Li$(p,n)^7$Be reaction. At this energy, all neutrons are emitted into a forward cone of 120° opening angle. The proton energy was calibrated by adjusting the maximum neutron energy of 106 keV via the time-of-flight method. This calibration step was carried out with the accelerator operated in pulsed mode, whereas the activation measurements were using the higher intensity dc beam. The LiF targets were layers 10 to 20 μm in thickness and 6 mm in diameter, evaporated onto 1.5-mm-thick Cu backings. Since the transmission of the copper backings was ≈98% in the energy range of interest, the effect of neutron scattering in the backing was negligible.

Under these conditions, integration of the neutron spectrum over the emission cone yields an almost perfectly

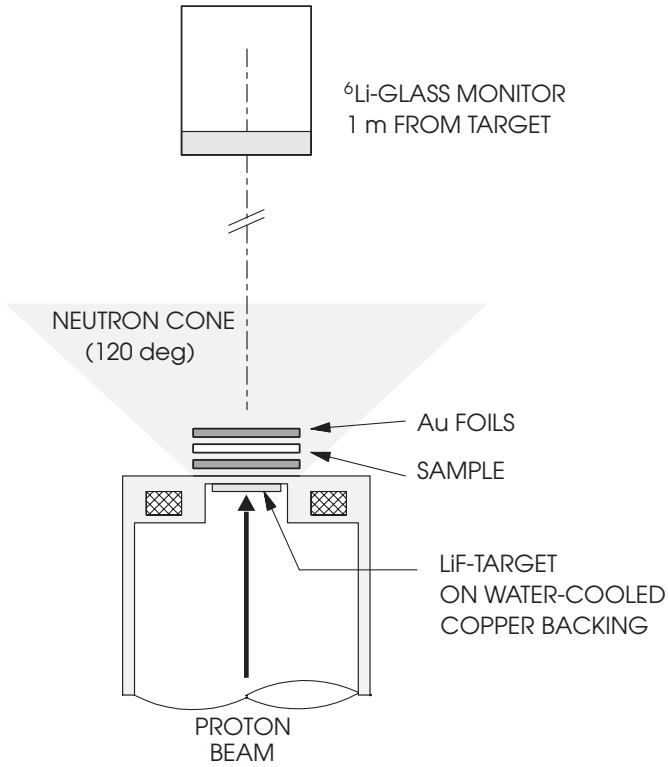

FIG. 2. Schematic sketch of the experimental setup.

Maxwell-Boltzmann distribution for a thermal energy of $kT = 25.0 \pm 0.5$ keV. Apart from minor corrections, activation in this spectrum provides a direct measurement of Maxwellian-averaged cross sections (MACS) at 25 keV thermal energy [23].

The activation measurements were performed at the Karlsruhe 3.7-MV Van de Graaff accelerator with dc beams between 80 and 100 μA, yielding an average neutron intensity of (1–3) $\times$ 10^9 s^{-1}. The samples were placed directly in front of the neutron target in the position of highest flux and entirely inside the neutron field. The samples were sandwiched between thin gold foils for determining the neutron fluence by means of the well-know neutron-capture cross section of ^{197}Au [23]. The experimental setup shown in Fig. 2.

Throughout all irradiations the neutron intensity was recorded with a ^{6}Li-glass monitor located on the proton beam axis at a distance of 1 m downstream from the lithium target in time steps of 60 s. This information is required to determine the correction factor f, by which the decay during the activation is taken into account, including the effect of fluctuations in the neutron yield (Sec. III).

B. Samples

The Yb, Os, and Hg samples were pellets pressed from natural oxide or chloride powder, whereas the Pt samples were cut from metal foils. Also the gold reference samples were made from 30-μm-thick metal foils. The isotopic abundances were adopted from Ref. [24] (see Table I). The ^{180}W sample was prepared from metal powder with 91.4 $\pm$ 0.3% enrichment. The samples were 6 and 10 mm in diameter. For each isotope several activations were performed with different experimental parameters, that is, by variation of sample dimensions (diameter and thickness) and irradiation times t_a. In this way it was possible to verify the related corrections and to obtain reliable information on systematic uncertainties. The characteristics of the samples and the respective irradiation times are summarized in Table II.

TABLE I. Sample materials and relative isotopic abundances [24].

Isotope	Sample material	Rel. abund. (%)	"Best"[a] (%)
^{168}Yb	Yb_2O_3	0.13(1)	0.127(2)
^{180}W	W (metal)	91.4(3)[b]	0.1198(2)
^{184}Os	OsO_2	0.02(1)	0.0197(5)
^{190}Pt	Pt (metal)	0.014(1)	0.013634(68)
^{196}Hg	Hg_2O	0.15(1)	0.15344(19)

[a]Best measurement from a single terrestrial source [24].
[b]Enriched sample. Natural isotopic abundance is 0.12(1).

C. Activity measurement

In total, 19 activations were carried out (see Table II). The activation times for ^{196}Hg were chosen to match the half-lives of the ground state and isomer in ^{197}Hg for determining the

TABLE II. Sample characteristics and irradiation times.

Sample	Diameter (mm)	Thickness (mm)	Mass (mg)	t_a (h)	Φ_{tot}[a] (10^{14} n)
		^{168}Yb$(n,\gamma)^{169}$Yb			
Yb-1	10	0.55	399.7	88.37	2.44
Yb-2	10	0.53	382.9	62.95	2.17
Yb-3	10	0.42	301.0	64.87	1.57
Yb-4	10	0.30	215.9	62.08	1.76
Yb-5	6	0.50	131.5	61.35	0.94
Yb-6	6	0.47	122.1	69.20	1.36
		^{180}W$(n,\gamma)^{181}$W			
W-1	6	0.09	50.0	44.55	1.25
		^{184}Os$(n,\gamma)^{185}$Os			
Os-1	10	0.55	496.8	65.50	2.66
Os-2	6	0.61	197.2	43.83	1.52
Os-3	6	0.31	99.4	40.28	1.00
		^{190}Pt$(n,\gamma)^{191}$Pt			
Pt-1	10	0.02	37.9	54.95	2.18
Pt-2	6	0.08	46.4	54.70	0.98
Pt-3	6	0.05	30.8	34.67	0.56
		^{196}Hg$(n,\gamma)^{197}$Hg and ^{196}Hg$(n,\gamma)^{197}$Hg^m			
Hg-1	10	0.88	494.0	45.75	1.01
Hg-2[b]	10	0.61	345.1	71.75	1.45
Hg-3	10	0.52	292.6	67.45	1.00
Hg-4[b]	6	0.83	167.7	45.85	1.10
Hg-5	6	0.56	114.1	42.67	0.67
Hg-6[b]	6	0.45	92.3	70.63	1.28

[a]Total neutron exposure during activation.
[b]Used for ^{196}Hg$(n,\gamma)^{197}$Hg^m.

TABLE III. Decay properties of the product nuclei. IT stands for "isomeric transition."

Isotope	$t_{1/2}$	E_γ (keV)	I_γ (%)	Reference
^{169}Yb	32.026(5) d	130.5	11.31(21)	[25]
		177.2	22.2(4)	
		198.0	35.8(7)	
		307.7	10.05(18)	
^{181}W	121.2(2) d	136.3	0.0311(10)	[26]
		152.3	0.083(3)	
^{191}Pt	2.802(25) d	359.9	6.4(5)	[27]
		538.9	15.9(12)	
^{197}Hg^{g}	64.14(5) h	77.4	18.7(4)	[28]
^{197}Hg^{m}	23.8(1) h	134.0 (IT)	33.48(26)	[28]
^{198}Au	2.69517(21) d	411.8	95.58(12)	[29]

total and partial (n,γ) cross sections. Only one activation could be performed on ^{180}W because the sample material was limited and the product nucleus ^{181}W was too long-lived for repeated activations.

After the irradiations, the induced activities of the investigated samples and of the gold foils were counted with high-purity Ge (HPGe) detectors. In all cases the most intense, pure γ-ray lines emitted in the decay of the product nuclei were used in the analysis. The decay properties of these lines are summarized in Table III.

Three HPGe detector setups were involved in γ counting: two single detectors with relative efficiencies of 30 and 100% and a 4π system of two HPGe Clover detectors of 130% each in very close geometry [30]. The small HPGe detector was used to count the significant activities of ^{198}Au, ^{169}Yb (two samples), ^{191}Os, and ^{197}Hg^{m}. The smaller activities of ^{169}Yb (four samples) were measured with the larger HPGe detector, and for the weak activities of isotopes with very low abundance or very weak γ-ray lines, the Clover system had to be employed (^{181}W, ^{191}Pt, and ^{197}Hg).

The efficiency of the detectors was determined in the investigated range of γ energies from 120 to 1408 keV with an uncertainty of 2% by a set of calibrated reference sources (Fig. 3). For the Clover system the efficiency calibration was complemented by detailed Monte Carlo simulations using the GEANT4 software [31,32], because some induced γ-ray lines were outside the range covered by the calibration sources. The simulated efficiency of the Clover system was normalized to fit the measured data points. The simulations were also necessary for determining the sample-related corrections in the close geometry of the Clover system as described below.

The counting position of the samples was reproducible within ± 0.1 mm by the use of special adaptors. This feature was particularly important for the close geometry of the Clover setup. Ambient backgrounds were reduced by a 10-cm-thick lead shield with an inner layer of 5-mm-thick copper. In all measurements the remaining γ-ray backgrounds were small and had practically no effect on the uncertainty of the final cross-section values.

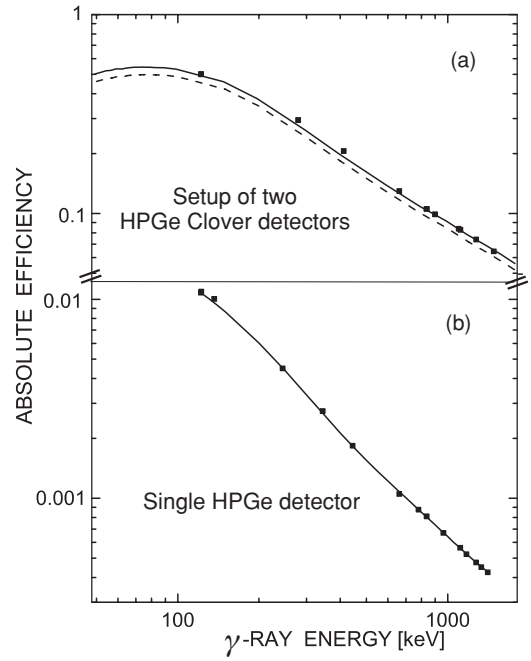

FIG. 3. Efficiency curves of the Clover detector system (a) and the single HPGe detector (b). The statistical uncertainties of the calibration measurements correspond to the size of the symbols. The simulated efficiency of the Clover system (dashed line) was normalized to fit the measured data points.

III. DATA ANALYSIS

A. General scheme

The total number of activated nuclei A at the end of the irradiation can be written as

$$A = \Phi_{\text{tot}} N \langle \sigma \rangle f, \tag{1}$$

where $\Phi_{\text{tot}} = \int_0^{t_a} \Phi(t) dt$ stands for the time-integrated neutron flux passing the sample during the irradiation, $\langle \sigma \rangle$ for the spectrum-averaged capture cross section, and N for the sample thickness [22].

The correction factor

$$f = \frac{\int_0^{t_a} \Phi(t) e^{-\lambda(t_a - t)} dt}{\int_0^{t_a} \Phi(t)\, dt} \tag{2}$$

is calculated from the neutron flux history $\Phi(t)$ recorded with the ^{6}Li glass detector and the decay rate λ of the product nucleus [22]. This correction accounts for the decay of activated nuclei during the irradiation time t_a as well as for variations of the neutron flux.

The number of counts C in a particular γ-ray line recorded during the measuring time t_m is proportional to the total number of activated nuclei A and can be written as

$$C = A K \epsilon_\gamma I_\gamma (1 - e^{-\lambda t_m}) e^{-\lambda t_w} \tag{3}$$

where ϵ_γ denotes the detector efficiency, I_γ the γ intensity per decay, and t_w the waiting time between irradiation and activity measurement [22]. The factor K describes the γ-ray self-absorption in the sample. For disk-shaped samples and

perpendicular radiation one has

$$K = \frac{1 - e^{-\mu x}}{\mu x}, \tag{4}$$

where μ is the γ-ray self-absorption coefficient and x the sample thickness [22]. This expression holds for the analysis of the γ spectra taken with the single HPGe detectors, where the distance between sample and detector was sufficiently large. The respective absorption coefficients μ were adopted from Ref. [33]. For the close geometry of the Clover system the absorption corrections had to be determined by GEANT4 simulations using a detailed model of the setup [30,32].

The corrections for coincidence summing and for the fact that the samples correspond to extended sources were calculated as described in Ref. [34]. For the small HPGe detector, these corrections were negligible due to the large distance between samples and detector and the small detector efficiency. For the large HPGe detector and Clover system these corrections were also obtained by GEANT4 simulations.

Since all measurements were carried out relative to gold, the neutron flux $\Phi_{\rm tot}$ cancels out in the cross-section ratio

$$\frac{\langle\sigma\rangle}{\langle\sigma\rangle_{\rm Au}} = \frac{A}{A_{\rm Au}}\frac{N_{\rm Au}}{N}\frac{f_{\rm Au}}{f}. \tag{5}$$

The reference value for the ^{197}Au cross section in the quasistellar spectrum of the ^{7}Li$(p,n)^{7}$Be reaction for $kT = 25$ keV of $\langle\sigma_{\rm exp}\rangle_{\rm Au} = 586 \pm 8$ mb was adopted from Ref. [23].

B. Discussion of uncertainties

The experimental uncertainties of the neutron-capture cross sections for the individual isotopes are summarized in Table IV. The contributions from the gold standard and from the detection efficiency ratio are common to all cases. The uncertainty of the Au standard includes the uncertainties of the gold cross section (1.4%), the γ-ray intensity (0.1%), and the counting statistics. As far as the detection efficiency is concerned, the 2% uncertainty corresponds to the efficiency ratio for the 411.8-keV line of gold and for the respective decay lines of the product nuclei. This ratio depends on the shape of the efficiency curves in Fig. 3 rather than on the absolute values.

In all cases, significant contributions are coming from the isotopic abundances [24]. For example in the case of ^{184}Os the "representative" isotopic abundance has a rather large uncertainty of 50% (see Table I) [24]. Because this value would overrun all other uncertainties we decided to use in all cases the "best measurements from a single terrestrial source" mentioned in Ref. [24]. Another large contribution are the line intensities in the case of ^{190}Pt. For ^{180}W, an additional 5% uncertainty was added because of the fact that the cross sections deduced from the two lines at 136 and 152 keV differ by more than the 6% uncertainty, which was expected from the quoted line uncertainties [26]. This discrepancy may indicate an inconsistency in the line intensities.

IV. RESULTS

In this section, the results of the present work are presented in tabular form with a short discussion of the various measurements. The comparison with previous results is given in Fig. 4 for the MACS $\langle\sigma\rangle_{kT}$ calculated on the basis of the measured $\langle\sigma_{\rm exp}\rangle$ reported here.

A. ^{168}Yb$(n,\gamma)^{169}$Yb

The six activations for the determination of the (n,γ) cross section of ^{168}Yb have been analyzed via the four strongest γ transitions in ^{169}Yb at 130.5, 177.2, 198.0, and 307.7 keV. As shown in Table V the individual results of all activations and all γ transitions are consistent within uncertainties, yielding a weighted average of $\langle\sigma_{\rm exp}\rangle = 1235 \pm 61$ mb.

B. ^{180}W$(n,\gamma)^{181}$W

Only one activation could be carried out for ^{180}W. In view of the very small natural abundance of ^{180}W of 0.12%, isotopically enriched material had to be used. In this case, the induced ^{181}W activity was limited because of the very weak γ-line intensities and the rather long half-life of ^{181}W. In addition, the signal to background ratio was challenged by interfering lines from the decay of the other tungsten isotopes.

TABLE IV. Compilation of uncertainties. "–" denotes negligible contributions.

Source of uncertainty	Related uncertainty (%)					
	^{168}Yb	^{180}W	^{184}Os	^{190}Pt	^{196}Hg^{m}	^{196}Hg$^{\rm tot}$
Au standard	1.4	1.4	1.4	1.4	1.4	1.4
Isotopic abundance	1.6	0.3	2.5	0.5	$\leqslant$0.2	$\leqslant$0.2
Ratio of γ efficiencies	2.0	2.0	2.0	2.0	2.0	2.0
Divergence of neutron flux	2.0	2.0	2.0	2.0	2.0	2.0
Intensity of γ lines	1.8–2.0	3.2–3.6	4.0	7.6–7.8	0.8	2.1
γ-ray self-absorption	$\leqslant$0.12	4.0	1.0	1.0–3.0	$\leqslant$0.2	1.0
Time factor f	–	–	–	0.5–0.7	0.8–1.3	$\leqslant$0.1
Half-life	$\leqslant$0.1	0.2	0.5	0.9	0.4	$\leqslant$0.1
Counting statistics	0.3–2.2	$\leqslant$0.4	$\leqslant$0.2	0.2–0.6	4–10	0.4–0.8
Total uncertainty	5.0	8.6[a]	7.3	9.1	5.4	5.3

[a]Including an additional uncertainty of 5% (see text).

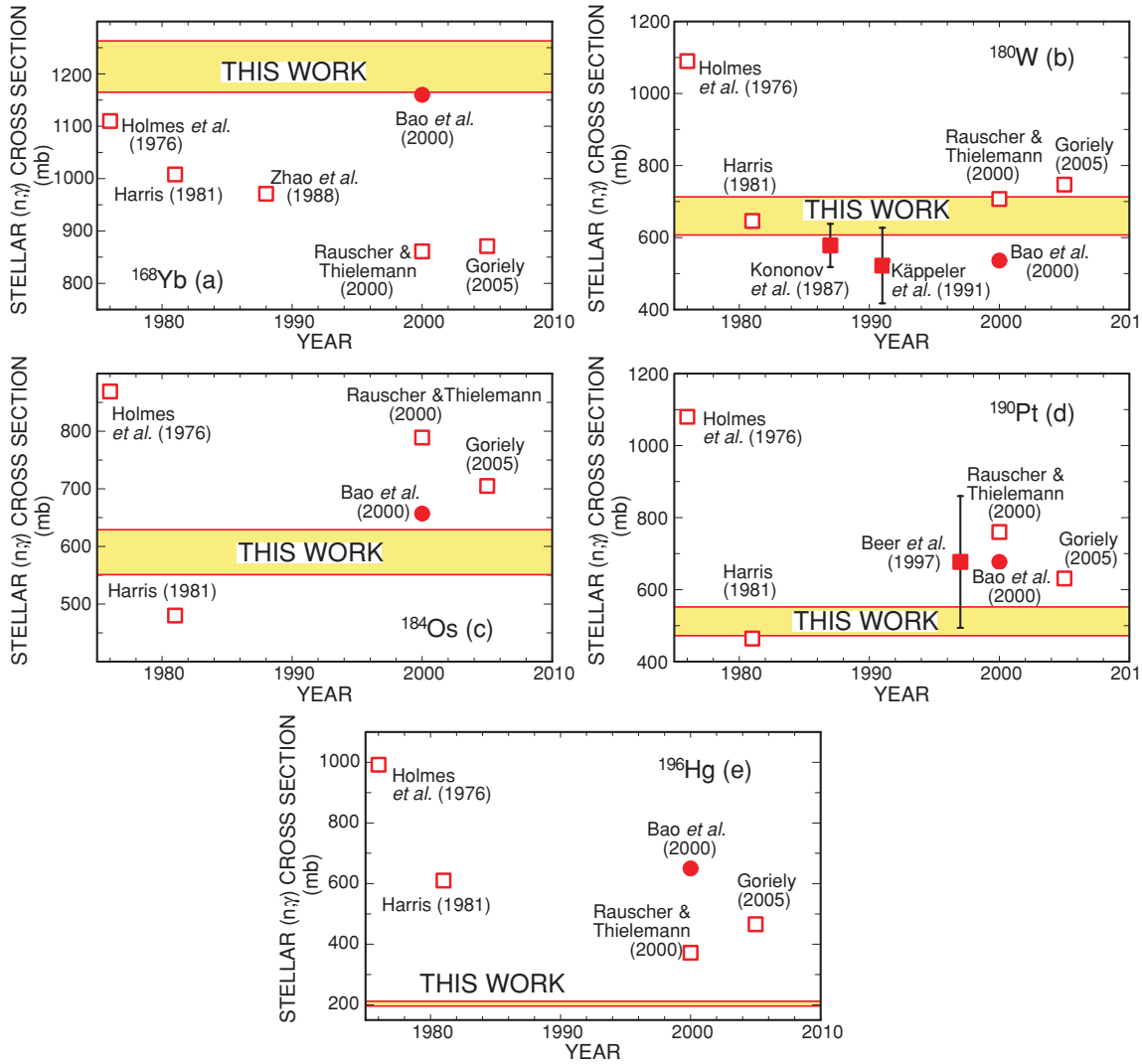

FIG. 4. (Color online) The present MACS for $kT = 30$ keV compared with previous data. Solid squares denote experimental results by Kononov *et al.* (1987) [43], Käppeler *et al.* (1991) [44], and Beer *et al.* (1997) [45]. Calculated data by Holmes *et al.* (1976) [39], Harris (1981) [40], Rauscher and Thielemann (2000) [19], and Goriely (2005) [21] are represented by open squares. The recommended values of the compilation by Bao *et al.* [13] are indicated by solid circles.

The ^{180}W$(n,\gamma)^{181}$W reaction has been analyzed via the two γ lines from ^{181}W at 136.3 and 152.3 keV (Table VI). The uncertainty of the weighted average was increased by an additional component of 5%, because the difference between the values deduced from the two γ lines was larger than expected from the individual uncertainties. Whether this difference is due to counting statistics or to inconsistent γ-ray intensities requires further investigation. The present weighted average is $\langle\sigma_{\rm exp}\rangle = 658 \pm 56$ mb.

TABLE V. Measured (n,γ) cross sections of ^{168}Yb.

Sample	$\langle\sigma_{\rm exp}\rangle$ (mb)			
	$E_\gamma = 130.5$ keV	177.2 keV	198.0 keV	307.7 keV
Yb-1	1225 ± 60	1324 ± 65	1344 ± 66	1332 ± 65
Yb-2	1229 ± 60	1261 ± 62	1260 ± 62	1265 ± 62
Yb-3	1212 ± 59	1283 ± 63	1344 ± 66	1301 ± 64
Yb-4	1137 ± 56	1191 ± 58	1274 ± 63	1214 ± 59
Yb-5	1211 ± 60	1216 ± 60	1233 ± 62	1188 ± 59
Yb-6	1127 ± 56	1151 ± 57	1255 ± 63	1170 ± 58
			Weighted average:	1235 ± 61

TABLE VI. Measured (n,γ) cross sections of ^{180}W.

Sample	$\langle\sigma_{\rm exp}\rangle$ (mb)	
	$E_\gamma = 136.3$ keV	152.3 keV
W-1	702 ± 47	620 ± 43
	Weighted average:	658 ± 56[a]

[a]Including an additional uncertainty of 5% (see text).

TABLE VII. Measured (n,γ) cross sections of ^{184}Os.

Sample	$\langle\sigma_{exp}\rangle$ (mb)
Os-1	603 ± 43
Os-2	577 ± 42
Os-3	578 ± 42
	Weighted average: 586 ± 42

C. ^{184}Os$(n,\gamma)^{185}$Os

The neutron capture cross section of ^{184}Os has been deduced from three activations with an overall uncertainty of 6.6%, which is dominated by the contributions from the intensity of the only useful γ transition at 646.1 keV. In this case there are no previous measurements to compare with the present weighted average of $\langle\sigma_{exp}\rangle = 586 \pm 42$ mb (Table VII).

D. ^{190}Pt$(n,\gamma)^{191}$Pt

The (n,γ) cross section of ^{190}Pt was determined in three activations via the γ-ray lines at 359.9 and 538.9 keV (Table VIII). As in the case of ^{184}Os, the accuracy of the weighted average of the ^{190}Pt cross section of 496 ± 43 mb is limited by the uncertainties of the respective γ intensities. The present weighted average is $\langle\sigma_{exp}\rangle = 496 \pm 45$ mb.

E. ^{196}Hg$(n,\gamma)^{197}$Hg

The partial (n,γ) cross sections of ^{196}Hg to the ground state and the isomeric state in ^{197}Hg were determined in six activations. The isomer ^{197}Hg^m decays predominantly to the ground state via isomeric transitions (IT, probability $91.4 \pm 0.7\%$) or with a smaller electron capture (EC) branch to ^{197}Au ($8.6 \pm 0.7\%$). Therefore, the partial cross section to the isomer, $\langle\sigma_{exp}\rangle^p$, has been deduced from the isomeric transition at 134.0 keV (Table IX).

The total neutron-capture cross section was determined in three of the activations via the 77.4-keV γ-ray transition in ^{197}Au. The counting started after a waiting time of about 10 days when the isomer ($t_{1/2} = 23.8$ h) had practically decayed. At this point the ground-state activity ($t_{1/2} = 64.14$ h) could be considered to represent the total cross section (apart from the small correction of 2.26 ± 0.21 mb for the EC decay of the isomer). The partial and total cross sections

TABLE VIII. Measured (n,γ) cross sections of ^{190}Pt.

Sample	$\langle\sigma_{exp}\rangle$ (mb)	
	$E_\gamma = 359.9$ keV	538.9 keV
Pt-1	503 ± 47	474 ± 42
Pt-2	518 ± 49	472 ± 42
Pt-3	523 ± 49	505 ± 44
	Weighted average: 496 ± 45	

TABLE IX. Measured partial and total (n,γ) cross sections of ^{196}Hg.

Sample	$\langle\sigma_{exp}\rangle^p$ to isomer[a] (mb) $E_\gamma = 134.0$ keV	$\langle\sigma_{exp}\rangle^{tot}$ (mb) 77.4 keV
Hg-1	25.5 ± 2.1	199 ± 10
Hg-2	28.0 ± 1.9	
Hg-3	23.1 ± 2.6	201 ± 10
Hg-4	26.5 ± 1.7	
Hg-5	27.3 ± 2.4	202 ± 10
Hg-6	25.7 ± 2.2	
Weighted averages	26.3 ± 1.4	201 ± 10

[a]Including 2.26 ± 0.21 mb correction for EC decay of isomer.

are $\langle\sigma_{exp}\rangle^p = 26.3 \pm 1.4$ and $\langle\sigma_{exp}\rangle^{tot} = 201 \pm 10$ mb, respectively (Table IX).

It is interesting to note that the isomeric ratio, $IR = \frac{\langle\sigma_{exp}\rangle^p}{\langle\sigma_{exp}\rangle^{tot}}$ increases from the thermal value $IR_{th} = 0.035 \pm 0.003$ [35] by a factor of 3 to 0.116 ± 0.007 at 25 keV neutron energy.

V. MAXWELLIAN-AVERAGED CROSS SECTIONS

A. General remarks

In an astrophysical environment with temperature T, interacting particles are quickly thermalized by collisions in the stellar plasma, and the neutron energy distribution can be described by a Maxwell-Boltzmann spectrum:

$$\Phi = dN/dE_n \sim \sqrt{E_n} \cdot e^{-E_n/kT}. \quad (6)$$

The experimental neutron spectrum of the ^{7}Li$(p,n)^7$Be reaction simulates the energy dependence of the flux $v \cdot \Phi \sim E_n \cdot e^{-E_n/kT}$ with $kT = 25.0 \pm 0.5$ keV almost perfectly [23]. The stellar-capture cross section at the energy kT is defined as

$$\langle\sigma\rangle_{kT} = \frac{2}{\sqrt{\pi}} \frac{\int_0^\infty \sigma(E_n)\, E_n\, e^{-E_n/kT}\, dE_n}{\int_0^\infty E_n\, e^{-E_n/kT}\, dE_n}, \quad (7)$$

where $\sigma(E_n)$ is the energy-differential cross section, E_n the neutron energy in the center-of-mass system, and $e^{-E_n/kT}$ the Boltzmann factor for the thermal energy kT. The factor $2/\sqrt{\pi}$ results from the normalization of the Maxwellian flux formula. Therefore, the measured cross sections could be transformed into MACS via

$$\langle\sigma\rangle_{kT} = \frac{2}{\sqrt{\pi}} \langle\sigma_{exp}\rangle \quad (8)$$

if the experimental neutron spectrum were of perfect Maxwellian shape. However, the energy cutoff at $E_n = 106$ keV and the small spectral differences between the experimental and the true thermal distribution require a correction for obtaining the exact MACS at $kT = 25$ keV from the measured data as well as for extrapolating these data to higher and lower thermal energies.

TABLE X. Normalization factors F_{norm} for the energy-dependent cross sections from data libraries or from theory.

	^{168}Yb	^{180}W	^{184}Os	^{190}Pt	^{196}Hg
JEFF 3.0/A	1.28	0.96	0.98	0.70	0.29
JENDL 3.3	–	–	–	–	5.93
ENDF-B/VII.0	–	–	–	–	5.92
NON-SMOKER	1.35	0.96	0.78	0.53	0.45

B. Calculation of MACS

The spectrum correction is obtained by using the new experimental results for normalizing the energy-dependent cross sections, $\sigma_{\text{eval}}(E_n)$, from evaluated data libraries. The normalization factor

$$F_{\text{norm}} = \langle\sigma_{\text{exp}}\rangle / \langle\sigma_{\text{eval}}\rangle \tag{9}$$

is determined by folding the evaluated cross section $\sigma_{\text{eval}}(E_n)$ with the experimental neutron spectrum. The MACS at kT is then

$$\langle\sigma\rangle_{kT} = \frac{2}{\sqrt{\pi}} \frac{\int_0^\infty [\sigma_{\text{eval}}(E_n)\, F_{\text{norm}}]\, E_n\, e^{-E_n/kT}\, dE_n}{\int_0^\infty E_n\, e^{-E_n/kT}\, dE_n}. \tag{10}$$

Evaluated cross sections were taken from the most recent versions of the available data libraries, that is, JEFF-3.0/A (Joint Evaluated Fission and Fusion General Purpose File, www.nea.fr/html/dbdata/JEFF/), JENDL-3.3 (Japanese Evaluated Nuclear Data Library [36], wwwndc.tokai-sc.jaea.go.jp/jendl/), and ENDF-B/VII.0 (Evaluated Nuclear Data File [37], www.nndc.bnl.gov/), which can be reached via the online database JANIS [38] (Java-Based Nuclear Information Software, www.nea.fr/janis/).

For ^{168}Yb, ^{180}W, ^{190}Pt, and ^{196}Hg the evaluated cross sections from JEFF-3.0/A have been used for the extrapolation to calculate the final MACS values. In case of ^{184}Os, where the evaluated cross section in JEFF-3.0/A is incomplete, the MACS have been determined from the energy dependence calculated with the statistical model code NON-SMOKER [19]. The normalization factors F_{norm} listed in Table X are reflecting either the uncertainties of previous data used in the evaluations (which are particularly large for ^{196}Hg) or the corresponding uncertainties of the adopted statistical model calculation.

TABLE XII. Ratio of MACS values based on the energy dependence of evaluated cross sections from the JEFF library and on the calculations with the statistical model code NON-SMOKER.

	Thermal energy (keV)			
	5	30	100	260
^{168}Yb	0.85	1.0	0.88	0.76
^{180}W	0.91	1.0	0.90	0.69
^{190}Pt	0.90	1.0	0.98	0.76
^{196}Hg	0.96	0.98	0.86	0.64

The final MACS are summarized in Table XI. The uncertainties quoted for the $kT = 30$ keV values correspond essentially to those of the measured cross sections, but increase gradually toward lower and higher thermal energies. From the differences in the energy-dependence between the evaluated cross sections from the JEFF library and the NON-SMOKER calculations summarized in Table XII, the additional uncertainty introduced by the extrapolation is estimated to reach about 10% at $kT = 5$ and 100 keV, but may be as large as 30% at 260 keV.

C. Comparison with previous values

The present MACS values at $kT = 30$ keV are compared in Fig. 4 with previous results. Because experimental data for ^{168}Yb did not exist, this work provides a significant improvement in accuracy compared to theoretical predictions. Among those, agreement is found with Ref. [39], whereas the ^{168}Yb cross section was underestimated in all other calculations [19,40–42].

TABLE XI. Final Maxwellian-averaged cross sections (in mb) for thermal energies $5 \leqslant kT \leqslant 260$ keV.

Thermal energy (keV)	^{168}Yb[a]	^{180}W[a]	^{184}Os[b]	^{190}Pt[a]	^{196}Hg[a]	^{196}Hg[c]
5	2997	1543	1564	1172	522	
10	2046	1061	1021	792	349	
15	1681	869	816	659	281	
20	1470	758	708	587	243	
25	1325	682	639	542	219	
30	1214(61)	624(54)	590(43)	511(46)	201(11)	26.3(1.4)
40	1053	538	524	469	178	
50	937	475	478	441	163	
60	850	426	445	421	151	
80	728	358	396	389	135	
100	649	313	364	363	123	
170	512	234	307	293	95	
260	448	198	283	234	75	

[a]Energy dependence from JEFF-3.0/A.
[b]Energy dependence from NON-SMOKER.
[c]Partial cross section given only for $kT = 30$ keV.

The present MACS of ^{180}W are higher than the previously reported measurements [43,44], but the three values are still compatible within uncertainties. In this case there is also good agreement with the theoretical predictions of Refs. [19,40,42].

For ^{184}Os there are no experimental data to compare with. Accordingly, the rather uncertain theoretical predictions can now be replaced by the significantly improved experimental result. This holds for ^{190}Pt as well, where the only previous measurement [45] was reported with a four times bigger uncertainty. The trend to overestimate the MACS for ^{184}Os and ^{190}Pt is even more pronounced in the theoretical predictions for ^{196}Hg.

In general, there is reasonable agreement with the compilation of Bao *et al.* [13] except for ^{196}Hg, where the present value is about three times smaller than previously recommended. However, this value, which represents a semiempirical estimate, does not fit the smooth trend defined by the experimental data of the even-even Hg isotopes (Fig. 5), in contrast to the present result. Figure 5 shows also that the slope of the NON-SMOKER data versus neutron number is too steep compared to that of the recommended values from the KADoNiS v0.3 database [17].

Apart from ^{180}W, the uncertainties could be improved by factors of 4 to 9 in all other cases. Accordingly, these results are essentially adopted in the KADoNiS database for nucleosynthesis in stars [17,46].

D. Impact on *p*-process network

Because most of the *p*-process reaction network involves unstable, neutron-deficient isotopes, theoretical calculations of the respective reaction rates are indispensable. The quality of the calculations, which are commonly based on the Hauser-Feshbach statistical model [19,42], depends strongly on the parameters used.

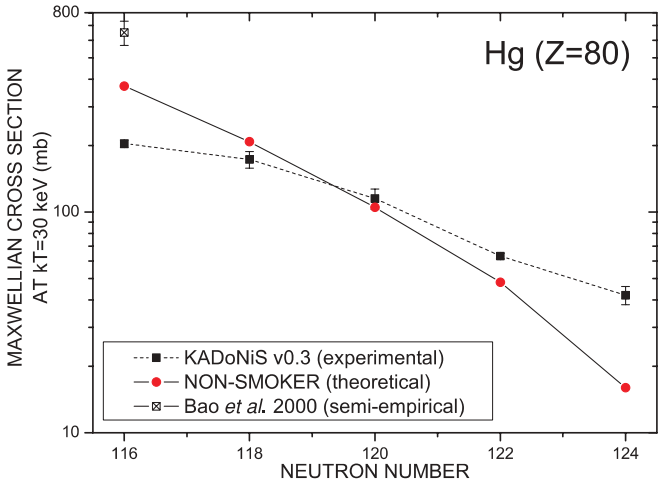

FIG. 5. (Color online) MACS at $kT = 30$ keV vs neutron number for the even-even Hg isotopes. The previously recommended value of ^{196}Hg of the compilation by Bao *et al.* (2000) [13] is indicated by the open square. The isotope chain for the NON-SMOKER predictions (red circles) exhibit a different slope compared to the new recommended values from KADoNiS v0.3 [17].

Experimental cross sections represent an important test for this parametrization. The present results for the *p* nuclei are particularly sensitive for the extrapolation to the neutron-deficient region. In view of their significantly improved accuracy, the cross section trends along the respective isotope chains are now much better defined, thus providing a more reliable basis for the MACS extrapolation with neutron number. This aspect will be addressed in more detail in a forthcoming article on cross-section measurements on the neutron-rich isotopes of Yb, W, Os, Pt, and Hg [47].

The impact of our new results and other recent neutron-capture measurements on *p*-process network calculations is briefly discussed in Refs. [16,48] and will be discussed in more detail in the upcoming third and final article of this series.

VI. SUMMARY

The rare *p* nuclei were long neglected in neutron-capture cross section campaigns because they were outside the reaction path of the *s*-process and also because isotopically enriched samples for time-of-flight measurements were not available with sufficient purity or sufficient amounts. Increasing interest in quantitative *p*-process studies motivated a series of activation measurements on the *p* nuclei in the mass region $A \geqslant 150$, where stellar (n,γ) cross sections were uncertain or completely missing.

In this work, 19 activations are reported in a quasistellar neutron spectrum corresponding to a thermal energy of $kT = 25$ keV. Systematic uncertainties and corrections applied in data analysis were investigated by variation of the relevant experimental parameters. Using gold as a reference, the cross sections of ^{168}Yb, ^{180}W, ^{184}Os, ^{190}Pt, and ^{196}Hg were determined with uncertainties of 4 to 8%, significantly more accurate than reported in the very few previous experiments on these isotopes.

The mere size of the *p*-process network and the fact that the vast majority of the involved isotopes are unstable restrict the possibility for direct cross-section measurements to comparably few selected cases. Therefore, cross-section calculations on the basis of the Hauser-Feshbach statistical model are indispensable in this context. Because the *p* nuclei are the most neutron-deficient stable isotopes, their cross sections are particularly suited to test and to optimize extrapolations into the *p*-process region. Further investigations of cross-section trends versus neutron number by additional measurements on neutron-rich isotopes are suggested.

ACKNOWLEDGMENTS

We thank M. Brock, E.-P. Knaetsch, D. Roller, and W. Seith for their continuous support during the irradiations at the Van de Graaff accelerator. Thanks are also due to E. Uberseder for his help with the GEANT simulations. One of us (J.M.) is indebted to KIT for financial support. I.D. acknowledges support by the Helmholtz society under Contract VH-NG 627.

[1] E. Burbidge, G. Burbidge, W. Fowler, and F. Hoyle, Rev. Mod. Phys. **29**, 547 (1957).
[2] K. Langanke and M. Wiescher, Rep. Prog. Phys. **64**, 1657 (2001).
[3] S. Woosley and W. Howard, Astrophys. J. Suppl. **36**, 285 (1978).
[4] S. Woosley and W. Howard, Astrophys. J. **354**, L21 (1990).
[5] M. Rayet, M. Arnould, M. Hashimoto, N. Prantzos, and K. Nomoto, Astron. Astrophys. **298**, 517 (1995).
[6] H. Schatz *et al.*, Phys. Rep. **294**, 167 (1998).
[7] H. Schatz, A. Aprahamian, V. Barnard, L. Bildsten, A. Cumming, M. Ouellette, T. Rauscher, F.-K. Thielemann, and M. Wiescher, Phys. Rev. Lett. **86**, 3471 (2001).
[8] S. Woosley, D. Hartmann, R. Hoffman, and W. Haxton, Astrophys. J. **356**, 272 (1990).
[9] C. Fröhlich, G. Martínez-Pinedo, M. Liebendörfer, F.-K. Thielemann, E. Bravo, W. R. Hix, K. Langanke, and N. T. Zinner, Phys. Rev. Lett. **96**, 142502 (2006).
[10] I. Dillmann, C. Domingo-Pardo, M. Heil, F. Käppeler, S. Walter, S. Dababneh, T. Rauscher, and F.-K. Thielemann, Phys. Rev. C **81**, 015801 (2010).
[11] W. Rapp, J. Görres, M. Wiescher, H. Schatz, and F. Käppeler, Astrophys. J. **653**, 474 (2006).
[12] C. Vockenhuber *et al.*, Phys. Rev. C **75**, 015804 (2007).
[13] Z. Bao, H. Beer, F. Käppeler, F. Voss, K. Wisshak, and T. Rauscher, At. Data Nucl. Data Tables **76**, 70 (2000).
[14] T. Rauscher, A. Heger, R. Hoffman, and S. Woosley, Astrophys. J. **576**, 323 (2002).
[15] I. Dillmann, M. Heil, F. Käppeler, T. Rauscher, and F.-K. Thielemann, Phys. Rev. C **73**, 015803 (2006).
[16] I. Dillmann, Ph.D. thesis, University of Basel, 2006.
[17] I. Dillmann and R. Plag, The Karlsruhe Astrophysical Database of Nucleosynthesis in Stars, Version 0.3, [http://www.kadonis.org], 2010.
[18] W. Hauser and H. Feshbach, Phys. Rev. **87**, 366 (1952).
[19] T. Rauscher and F.-K. Thielemann, At. Data Nucl. Data Tables **75**, 1 (2000).
[20] T. Rauscher and F.-K. Thielemann, At. Data Nucl. Data Tables **79**, 47 (2001).
[21] S. Goriely, Hauser-Feshbach Rates for Neutron Capture Reactions (version 08/26/05) [http://www-astro.ulb.ac.be/Html/hfr.html], 2005.
[22] H. Beer and F. Käppeler, Phys. Rev. C **21**, 534 (1980).
[23] W. Ratynski and F. Käppeler, Phys. Rev. C **37**, 595 (1988).
[24] J. De Laeter, J. Böhlke, P. de Bievre, H. Hidaka, H. Peiser, K. Rosman, and P. Taylor, Pure Appl. Chem. **75**, 683 (2003).
[25] V. Shirley, Nucl. Data Sheets **64**, 505 (1991).
[26] S.-C. Wu, Nucl. Data Sheets **106**, 367 (2005).
[27] V. Vanin, N. Maidana, R. Castro, E. Achterberg, O. Capurro, and G. Marti, Nucl. Data Sheets **108**, 2393 (2007).
[28] X. Huang and C. Zhou, Nucl. Data Sheets **104**, 283 (2005).
[29] Z. Chunmei, Nucl. Data Sheets **95**, 59 (2002).
[30] M. Heil, S. Dababneh, A. Juseviciute, F. Käppeler, R. Plag, R. Reifarth, and S. O'Brien, Phys. Rev. C **71**, 025803 (2005).
[31] S. Agostinelli *et al.*, Nucl. Instrum. Methods A **506**, 250 (2003).
[32] S. Dababneh, N. Patronis, P. Assimakopoulos, J. Görres, M. Heil, F. Käppeler, D. Karamanis, S. O'Brien, and R. Reifarth, Nucl. Instrum. Methods A **517**, 230 (2004).
[33] M. Berger, J. Hubbell, S. Seltzer, J. Chang, J. Coursey, R. Sukumar, and D. Zucker, XCOM: Photon Cross Sections Database, NIST Standard Reference Database 8, National Institute of Standards and Technology [http://physics.nist.gov/PhysRefData/Xcom/Text/XCOM.html], 2008.
[34] K. Debertin and R. Helmer, *Gamma- and X-Ray Spectrometry with Semiconductor Detectors* (North-Holland, Amsterdam, 1989).
[35] S. Mughabghab, *Atlas of Neutron Resonances* (Elsevier, Amsterdam, 2006), 5th ed.
[36] K. Shibata, T. Kawano, and T. Nakagawa, Japanese Evaluated Nuclear Data Library, Version 3, Revision 3: JENDL. 3.3, J. Nucl. Sci. Technol. **39**, 1125 (2002).
[37] M. Chadwick *et al.*, Nucl. Data Sheets **107**, 2931 (2006).
[38] N. Soppera, M. Bossant, H. Henriksson, P. Nagel, and Y. Rugama, in *International Conference on Nuclear Data for Science and Technology, Nice, France, 2007*, edited by O. Bersillon, F. Gunsing, E. Bauge, R. Jacqmin, and S. Leray (EDP Sciences, Les Ulis, 2008), p. 773.
[39] J. Holmes, S. Woosley, W. Fowler, and B. Zimmerman, At. Data Nucl. Data Tables **18**, 305 (1976).
[40] M. Harris, Astrophys. Space Sci. **77**, 357 (1981).
[41] Z. Zhao, D. Zhou, and D. Cai, in *Nuclear Data for Science and Technology*, edited by S. Igarasi (Saikon, Tokyo, 1988), p. 513.
[42] S. Goriely, technical report (unpublished), 1998 [http://www-astro.ulb.ac.be].
[43] V. Kononov, E. Poletaev, V. Timokhov, G. Manturov, M. Bokhovko, and A. Voevodskii, Sov. J. Nucl. Phys. **46**, 33 (1987).
[44] F. Käppeler, S. Jaag, Z. Bao, and G. Reffo, Astrophys. J. **366**, 605 (1991).
[45] H. Beer, P. Mohr, H. Oberhummer, T. Rauscher, P. Mutti, F. Corvi, P. Sedyshev, and Y. Popov, in *Interaction of Neutrons with Nuclei*, edited by W. Furman (JINR, Dubna, 1997), p. 229.
[46] I. Dillmann, M. Heil, F. Käppeler, R. Plag, T. Rauscher, and F.-K. Thielemann, AIP Conf. Proc. **819**, 123 (2005).
[47] J. Marganiec, I. Dillmann, C. Domingo-Pardo, M. Heil, and F. Käppeler (to be published).
[48] I. Dillmann, T. Rauscher, M. Heil, F. Käppeler, W. Rapp, and F.-K. Thielemann, J. Phys. G: Nucl. Part. Phys. **35**, 014029 (2008).